

Infrared-excess white dwarfs in the *Gaia* 100 pc sample

A. Rebassa-Mansergas^{1,2*}, E. Solano^{3,4}, S. Xu⁵, C. Rodrigo^{3,4},
F. M. Jiménez-Esteban^{3,4}, S. Torres^{1,2}

¹ *Departament de Física, Universitat Politècnica de Catalunya, c/Esteve Terrades 5, 08860 Castelldefels, Spain*

² *Institut d'Estudis Espacials de Catalunya, Ed. Nexus-201, c/Gran Capità 2-4, 08034 Barcelona, Spain*

³ *Departamento de Astrofísica, Centro de Astrobiología (CSIC-INTA), ESAC Campus, Camino Bajo del Castillo s/n, E-28692 Villanueva de la Cañada, Madrid, Spain*

⁴ *Spanish Virtual Observatory, E-28692 Villanueva de la Cañada, Madrid, Spain*

⁵ *Gemini Observatory, 670 N. A'ohoku Place, Hilo, HI 96720*

Accepted XXX. Received YYY; in original form ZZZ

ABSTRACT

We analyse the 100 pc *Gaia* white dwarf volume-limited sample by means of VOSA (Virtual Observatory SED Analyser) with the aim of identifying candidates for displaying infrared excesses. Our search focuses on the study of the spectral energy distribution (SED) of 3,733 white dwarfs with reliable infrared photometry and $G_{BP} - G_{RP}$ colours below 0.8 mag, a sample which seems to be nearly representative of the overall white dwarf population. Our search results in 77 selected candidates, 52 of which are new identifications. For each target we apply a two-component SED fitting implemented in VOSA to derive the effective temperatures of both the white dwarf and the object causing the excess. We calculate a fraction of infrared-excess white dwarfs due to the presence of a circumstellar disk of $1.6 \pm 0.2\%$, a value which increases to $2.6 \pm 0.3\%$ if we take into account incompleteness issues. Our results are in agreement with the drop in the percentage of infrared excess detections for cool ($< 8,000$ K) and hot ($> 20,000$ K) white dwarfs obtained in previous analyses. The fraction of white dwarfs with brown dwarf companions we derive is $\approx 0.1 - 0.2\%$.

Key words: (stars:) white dwarfs – (stars:) circumstellar matter – (stars:) brown dwarfs – (astronomical data bases:) virtual observatory tools

1 INTRODUCTION

Low- and intermediate-mass main sequence stars ($M \lesssim 8 \sim 11 M_{\odot}$) end their lives as white dwarfs (WDs; e.g. Siess 2007). WDs are hence the most common stellar remnants and are one of the most common objects in the Galaxy. Given that WDs are compact objects and nuclear reactions have ceased in their interiors, their structure is supported by the pressure of the degenerate electrons in their cores. The energy reservoir available from previous evolutionary phases is contained within this degenerate core and radiated away through a thin envelope of non-degenerate matter following a moderately well-understood cooling process (see e.g. the review by Althaus et al. 2010 and reference therein for a thorough discussion of this issue). This envelope is generally formed by an upper layer of hydrogen of $10^{-2} - 10^{-4} M_{\odot}$ and a lower layer of helium of $10^{-15} - 10^{-5} M_{\odot}$ (see e.g. Castanheira & Kepler 2008; Tremblay & Bergeron 2008). Due to the high surface grav-

ity acting on WD atmospheres, the heavier elements sink towards the deep interiors. Hence, the optical spectra of the majority of WDs show Balmer absorption lines typical of hydrogen-rich atmospheres, or helium absorption lines if this hydrogen layer is lost (Bergeron et al. 2011; Koester & Kepler 2015). However, 25-50 per cent of WDs show heavy elements apart from hydrogen and helium (Zuckerman et al. 2003; Koester et al. 2014). These WDs are referred to as DAZs and DBZs, respectively, or DZs if only metal lines are observed. It is of vital importance to understand how these metals reached the atmosphere of those WDs.

Planets and minor planets located a few AUs away from a host star are expected to survive the giant phases once the star evolves out of the main sequence and becomes a WD (Burleigh et al. 2002; Jura 2008). This implies the orbits of these planets expand, a rearrangement that causes instability to the system. This perturbation may cause some of the surviving minor planets to enter into the tidal radius of the WD and, as a consequence, to be disrupted and accreted (Debes & Sigurdsson 2002;

* E-mail: alberto.rebassa@upc.edu

(Debes et al. 2012) during a process that can last a few Gyrs (Bonsor et al. 2011; Veras et al. 2013). The accretion of planetary material leads to the enrichment of heavy elements in the atmosphere of the WD, explaining the identification of metal transitions in the spectra of such DZ WDs. An additional observational feature that arises as a consequence of the disruption of a minor planet is a dust and/or a gas disk within the tidal radius of the WD (Gänsicke et al. 2006; Xu & Jura 2012; Dennihy et al. 2018). It has been observed that some of these dusty WDs are dynamically active (Xu & Jura 2014) and recently, transits from an actively disintegrating asteroid have been discovered for the first time around a dusty WD (Vanderburg et al. 2015). The observational feature of dust disks around WDs is the detection of infrared (IR) excess (e.g. Zuckerman & Becklin 1987). Apart from a few exceptions (Xu et al. 2015; Wilson et al. 2019), the great majority of dusty WDs display also traces of heavy elements in their atmospheres. The dust disk occurrence is about 1–4% for WDs (Barber et al. 2012; Rocchetto et al. 2015; Wilson et al. 2019). For less than 0.5% of the cases, the excess arises from the existence of a sub-stellar brown dwarf companion (Farihi & Christopher 2004; Farihi et al. 2005). It is also possible that the IR-excess arises from the presence of low-mass star companions that are outshined in the optical by the flux of a relatively hot WD (Rebassa-Mansergas et al. 2010; Badenes et al. 2013; Rebassa-Mansergas et al. 2016).

The presence of metals in the atmosphere of a WD provides unique information about the composition of the accreted material (Klein et al. 2010; Gänsicke et al. 2012; Xu et al. 2014; Hollands et al. 2018a), which is found to be chemically Earth-like (Wilson et al. 2016). Pollution rich in water (Farihi et al. 2013; Raddi et al. 2015) as well as water/ice-rich and volatile-rich (C & N) (Xu et al. 2017) has also been observed. Unfortunately, the current number of *confirmed* WDs by Spitzer observations displaying infrared excess due to a circumstellar disk is just 35 (see the recent review by Farihi 2016 and reference therein), which makes it difficult to characterise the properties of extreme planetary systems. In this work we aim at identifying additional IR-excess WD candidates, in particular those with a circumstellar disk, by analysing the most complete and volume-limited sample of WDs to date, identified thanks to the data provided by the second release of the *Gaia* mission.

2 IDENTIFICATION OF INFRARED-EXCESS WHITE DWARF CANDIDATES

The data provided by the *Gaia* satellite through its Second Data Release has allowed identifying unprecedented samples of both single and binary WDs (e.g. El-Badry & Rix 2018; Gentile Fusillo et al. 2019), as well as compiling the largest and most complete volume-limited catalogue of such objects to date within 100 pc (Jiménez-Esteban et al. 2018). In order to identify WDs with IR excess we took the sample of Jiménez-Esteban et al. (2018) of 8,555 objects at less than 100 pc and with $G_{BP} - G_{RP}$ colours below 0.8 mag available at "The SVO archive of White Dwarfs from *Gaia*"¹.

¹ <http://svo2.cab.inta-csic.es/vocats/v2/wdw/>

This colour cut is equivalent to excluding WDs cooler than 6,000 K and it is required due to the expected large contamination of non-WDs at lower effective temperatures (see Jiménez-Esteban et al. 2018 for details). We analysed the Spectral Energy Distributions (SEDs) of the 8,555 WDs taking advantage of VOSA² (Virtual Observatory SED Analyser; Bayo et al. 2008). VOSA is a Virtual Observatory tool that allows building the SEDs of thousands of objects in an automated way from a large number of photometric catalogues ranging from the ultraviolet to the infrared. VOSA compares the photometric data with different collections of theoretical models and determines which model best reproduces the observed data following different statistical approaches. Physical parameters (e.g. effective temperatures, luminosities) are then estimated for each WD from the model that best fits the data. VOSA also allows the identification of IR-excess in the SED and estimates the effective temperature and luminosity of the source causing the excess, which together with the Stefan-Boltzmann equation yields also its radius. Note that the calculated radius has physical meaning only when the source of excess is a companion.

In this paper we made use of the following photometric catalogues available at VOSA: GALEX (Bianchi & GALEX Team 2000), *Gaia* DR2 (Gaia Collaboration et al. 2018), SDSS DR12 (Alam et al. 2015), Pan-STARRS DR1 (Chambers et al. 2016), the Dark Energy Survey (DES) (Dark Energy Survey Collaboration et al. 2016), 2MASS PSC (Skrutskie et al. 2006), VISTA (Cross et al. 2012), UKIDSS (Hewett et al. 2006), and WISE (Wright et al. 2010). Additionally, we made use of the Spitzer Enhanced Imaging Products (SEIP) catalogue (Wu et al. 2010), which is presently not included in VOSA. To avoid potential mismatches we used the *Gaia* proper motions to calculate the corresponding *Gaia* coordinates at the J2000 epoch, used by all other surveys considered³.

From the original list, we filtered out objects with less than three reliable IR ($>12,000\text{\AA}$) photometric points in their SEDs. Reliable photometry implies data not affected by contamination from nearby sources, artifacts or quality flag issues (Qflg \neq U in the J and H bands for 2MASS; ccf=0 and qph=A/B in the W2 band for WISE; ppErrBits $<$ 256 for both VISTA and UKIDSS). This resulted in 3,733 selected *Gaia* WDs. In order to explore the possibility that our selected sample is representative of the overall WD population we compared the corresponding WD effective temperature and mass distributions (see Section 5 for details on how these parameters are derived) to those arising from the catalogue of *Gaia* DA WDs within 20 pc of Hollands et al. (2018b). This is not only a volume-limited and complete sample, but also all 20 pc WDs have available effective temperature

² <http://svo.cab.inta-csic.es/theory/vosa/>

³ Ideally, for high proper motion objects one would require to work out the *Gaia* coordinates at the exact epoch of observations of the other different surveys. However, VOSA uses a search radius of 5", which means a WD needs a proper motion higher than 330 mas/year to move more than 5" in 15 years (J2000 to J2015). Less than 1% of the 8,555 WDs within 100pc from Jiménez-Esteban et al. (2018) have such high proper motions. Therefore, not calculating the *Gaia* coordinates at the exact epoch of observations of the other surveys has a very low impact.

Table 1. List of the 26 co-moving WD+M systems found in this work. Coordinates, parallaxes and proper motions are from *Gaia* DR2. The object names are obtained from Simbad and the effective temperatures have been estimated as described in Sect 2. * in the second last column indicates that we were not able to estimate T_{eff} due to the lack of enough good photometric points to run the SED fitting. In these cases, the spectral types for the cool components were estimated using the $G-G_{\text{RP}}$ colour and the calibration provided by Pecaut & Mamajek (2013).

ID	Gaia ID DR2	RA(ICRS) deg	DEC(ICRS) deg	Name	Parallax mas	PMRA mas/yr	PMDE mas/yr	T_{eff} K	comment
1A	396370097820352256	22.4283	42.4715	GD 13	11.88±0.09	94.49±0.12	-45.59±0.11	22,000	(1)
1B	396370093526060672	22.4271	42.4704		11.39±0.17	92.30±0.21	-45.30±0.24	2,900	
2A	5119295082016649472	37.3367	-24.4348		13.05±0.05	91.76±0.1	-94.85±0.10	15,500	(1)
2B	5119295082017370368	37.3359	-24.4350		13.14±0.06	89.27±0.11	-98.94±0.12	3,200	
3A	18493721155296768	39.6289	6.6333	PG 0235+064	16.89±0.06	-12.77±0.09	-90.99±0.08	13,000	(1)
3B	18493721155296640	39.6283	6.6353	2MASS J02383078+0638071	16.98±0.07	-11.22±0.11	-87.69±0.10	3200	
4A	16426811093797760	51.5877	11.5158		16.38±0.06	-49.14±0.12	-36.06±0.08	17,500	(1)
4B	16426806798453632	51.5884	11.5149	[ZEH2003] RX J0326.3+1131 3	16.12±0.08	-44.65±0.18	-35.08±0.12	M2V*	
5A	166587938734739456	64.1762	32.1891	SDSS J041642.29+321120.5	10.13±0.09	0.86±0.17	-83.38±0.13	8250	(2)
5B	166587938734739328	64.1769	32.1891		10.42±0.16	2.16±0.32	-80.71±0.23	3100	
6A	4811421896276768128	73.3033	-44.3944		11.13±0.04	26.87±0.07	23.22±0.08	WD*	(1)
6B	4811421896275732480	73.3026	-44.3937		11.17±0.08	25.32±0.16	23.01±0.18	M4-5V*	
7A	201854258801563520	74.1309	41.5220		10.13±0.09	-36.68±0.16	-106.43±0.11	9,500	(1)
7B	201854258801564288	74.1293	41.5218		10.09±0.07	-35.79±0.13	-106.98±0.09	3,300	
8A	3439162768415866112	96.5553	32.2198		12.58±0.06	-17.35±0.11	-38.63±0.1	11,000	(1)
8B	3439162768415865600	96.5566	32.2202		12.71±0.11	-19.45±0.20	-37.31±0.18	3,200	
9A	5598661329740179712	116.5578	-30.4313		14.49±0.05	59.43±0.07	-117.24±0.08	17,500	(1)
9B	5598661329740179584	116.5575	-30.4305		14.39±0.06	59.54±0.09	-117.89±0.1	3,100	
10A	3842126835031738368	137.9023	-0.2159		16.80±0.19	59.78±0.29	-36.23±0.25	6,250	(1)
10B	3842126835031738496	137.9020	-0.2144		16.66±0.21	56.93±0.36	-35.10±0.29	2,800	
11A	1075673567146680576	170.0952	72.8795		11.50±0.06	-63.50±0.10	5.56±0.09	15,750	(1)
11B	1075673567146680704	170.0922	72.8795		11.60±0.06	-64.37±0.11	3.08±0.09	3,600	
12A	1692021543289085184	190.5089	75.1460	PG 1240+754	12.42± 0.05	-201.85±0.08	-35.09±0.07	WD*	(3)
12B	1692021543289084672	190.5142	75.1450	G 255-B18B	11.98±0.06	-199.77±0.11	-32.49±0.09	3200	
13A	1552488776081383040	204.0067	48.4793	GD 325	27.09±0.04	-134.10±0.04	-42.98±0.05	17,500	(1)
13B	1552488776081383168	204.0079	48.4796		27.06±0.06	-127.55±0.07	-47.55±0.09	3,000	
14A	1604422214954487168	216.6841	50.1066	CBS 268	15.28±0.04	-10.60±0.06	-82.72±0.06	15,250	(4)
14B	1604422283673964160	216.6830	50.1093		15.20±0.04	-11.70±0.06	-84.83±0.06	3,300	
15A	1276054682231244160	225.4845	30.3831	PG 1459+306	15.00±0.04	-43.15±0.04	52.77±0.06	19,250	(1)
15B	1276054677930790272	225.4851	30.3842		14.94±0.03	-37.31±0.03	54.16±0.04	3,500	
16A	1643551566043342848	240.7042	67.4912		12.28±0.08	-25.19±0.15	6.98±0.13	8,000	(1)
16B	1643551566043342592	240.7044	67.4898		12.32±0.03	-24.36±0.06	4.07±0.05	3,500	
17A	4457170451083163392	242.7226	11.7313	PG 1608+119	11.59±0.06	36.49±0.07	-12.99±0.06	20,000	(1)
17B	4457170446785639424	242.7218	11.7316		11.58±0.05	33.30±0.06	-13.97±0.05	3,500	
18A	1300356053864952064	251.6571	25.3068		12.32±0.05	-44.96±0.07	2.40±0.11	12,750	(1)
18B	1300356809779196288	251.6561	25.3070		12.25±0.06	-43.78±0.09	3.70±0.13	3,100	
19A	4360643809885839232	257.3352	-7.8785		13.82±0.08	-37.94±0.13	-112.47±0.09	17,750	(1)
19B	4360643809885838976	257.3362	-7.8790		13.91±0.06	-41.21±0.10	-110.21±0.07	3,400	
20A	4366961260100103680	260.7060	-2.8049		12.34±0.09	-17.64±0.16	-29.71±0.13	7,250	(4)
20B	4366961260100103552	260.7054	-2.8054		11.87±0.07	-19.20±0.11	-29.08±0.09	3,200	
21A	5803547624984209792	266.1464	-72.9932		11.43±0.05	14.44±0.06	17.53±0.08	WD*	(4)
21B	5803547624984209664	266.1488	-72.9932		11.36±0.10	16.45±0.11	14.49±0.15	M5V*	
22A	2103614787618232192	284.3691	40.5932		15.00±0.03	-23.46±0.05	41.47±0.05	17,500	(1)
22B	2103614787618232448	284.3697	40.5938	KIC 5342558	15.12±0.05	-26.09±0.09	42.79±0.09	3,100	
23A	1768730586908531712	330.3371	15.0917		10.68±0.06	-30.32±0.11	-89.21±0.10	14,250	(1)
23B	1768730586908531840	330.3375	15.0928		10.63±0.04	-30.56±0.07	-88.05±0.06	3,500	
24A	2811484217573797248	347.3354	11.5747		14.33±0.20	23.92±0.35	-62.61±0.25	7,000	(1)
24B	2811484217572663168	347.3361	11.5753		14.37±0.17	24.35±0.31	-65.31±0.21	2,900	
25A	6393502099375879552	348.2538	-64.3321		12.71±0.05	179.05±0.07	23.96±0.08	WD*	(4)
25B	6393502099376815744	348.2521	-64.3322		13.36±0.24	184.32±0.34	19.37±0.36	M3-4V*	
26A	1999127510441929600	356.2808	58.2209		10.22±0.08	28.87±0.11	5.83±0.08	11,750	(4)
26B	1999127510436274048	356.2794	58.2205		10.54±0.39	29.84±0.61	5.69±0.42	2,800	

(1) El-Badry & Rix (2018); (2) Ren et al. (2014); (3) Simbad; (4) This work.

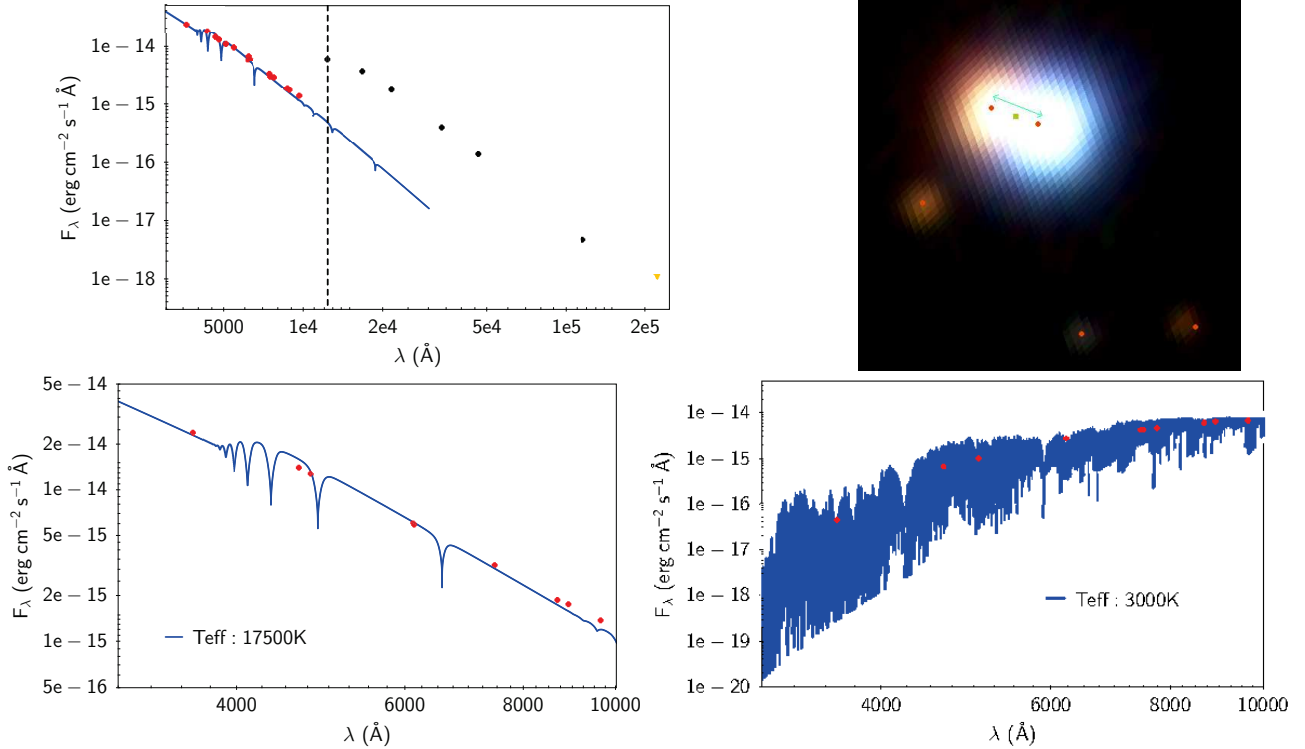


Figure 1. Top left: Example of a composite SED of GaiaID: 1075673567146680576 and GaiaID:1075673567146680704 (IDs 11A and 11B in Table 1). The abrupt jump at IR wavelengths indicates that more than one object is contributing to the stellar flux. The vertical dashed line marks the wavelength at which VOSA detects *excess* (understood as a significant change in the slope and/or a clear deviation from the photospheric flux predicted by the model). The yellow inverted triangle indicates that the photometric value is an upper limit. Top right: SDSS image showing two partially resolved objects. Red bullets represent SDSS sources while the green square indicates the position of the single WISE catalogue entry for the two sources. Bottom panels: The SEDs of the individual objects built using photometry from surveys of higher spatial resolution (SDSS, PanStarrs) along with the best fit models and their associated effective temperatures. Photometric errors are too small to be seen.

and mass determinations. Kolmogorov-Smirnov (KS) tests yield probabilities of 10^{-5} (4.4σ ; effective temperature) and 0.55 (0.6σ ; mass) for our and the 20 pc *Gaia* samples to be drawn from the same parent population. If we exclude cool ($<6,000\text{K}$) WDs from the 20 pc sample, the effective temperature KS probability increases to 0.16 (1.4σ). We thus conclude there are no strong indications for our sample not to be representative of the overall WD population, except at effective temperature values under 6,000 K. The lack of such cool WDs in our sample is not surprising since these are excluded by our imposed $G_{\text{BP}} - G_{\text{RP}} < 0.8$ colour cut.

The observational SEDs of the 3,733 selected objects were compared to the hydrogen-rich WD collection of theoretical model atmosphere spectra of Koester (2010) (see Sect. 4.1 in Jiménez-Esteban et al. 2018 for a detailed description of the main characteristics of this grid of models) to identify IR excesses. To that end, VOSA first executes an iterative algorithm which is an extension of the method described in Lada et al. (2006). Starting at $\lambda \geq 21500\text{Å}$, VOSA computes the slope of the linear regression of the observational SED in a $\log \nu F_\nu$ vs. $\log \nu$ diagram. This slope is recomputed by adding new infrared photometric points at every step. If, in any of these steps, the slope becomes significantly smaller (< 2.56) than the one expected from a stellar photospheric emission, VOSA flags the object as potentially affected by IR excess and photometric points at longer wave-

lengths are not taken into account in the SED fitting process for deriving the WD effective temperature and luminosity.

Once the SED fitting is completed, VOSA performs a further refinement of the IR excess estimation by comparing, for each photometric point, the observational flux to the synthetic flux obtained from the model that best fits the data. Significant ($> 3\sigma$) deviations in the observational flux are flagged by VOSA as potential IR excesses. A detailed description of how VOSA manages the infrared excess can be found in the VOSA documentation⁴. After this process, VOSA identified 377 WD candidates to show IR-excess among our initial 3,733 objects.

In a first step, we visually inspected the optical (PanSTARRS1, SDSS and DSS) and IR (2MASS and WISE) images of the 377 sources using Aladin⁵ (Bonnarel et al. 2000). The VOSA SED fittings were also checked. We removed a total of 221 sources (58%) from our target list mainly due to the WISE poor spatial resolution ($6''$ beam size), which causes a significant number of false positives due to contamination by nearby sources. This contamination rate is slightly lower to that found by other authors (75%, e.g. Barber et al. 2016). Of the remaining 156 objects, 38 were identified as

⁴ <https://bit.ly/2KRCv9x>

⁵ <http://aladin.u-strasbg.fr>

co-moving systems by using *Gaia* parallaxes and proper motions, as well as photometry from surveys where the components of the systems appear spatially resolved. Most of these objects can be easily identified by the jump in their SEDs at IR (mainly WISE) wavelengths. This jump is caused by the sum of the fluxes of the nearby sources that form the system due to the WISE spatial resolution (see an example in Figure 1). 26 of the 38 co-moving pairs were identified as WD+M systems, most of them already reported by [El-Badry & Rix \(2018\)](#) (see Table 1). Effective temperatures were estimated using VOSA and the [Koester \(2010\)](#) and BT-Settl ([Allard et al. 2012](#)) models for the WD and the M star components, respectively. The other 12 systems are reported in Table 2.

Of the remaining 118 WDs, one has associated two entries in the *Gaia* DR2 catalogue separated by less than $2''$ (Gaia IDs: 883243467325018496 / 883243467323599616). The differences in parallaxes and the SED analysis made with VOSA conclude that the secondary component causing the IR excess is, most likely, a background M giant. Similar cases are the sources 2612592841965015424, 2564424130905288192, 63846445499673472, 2969841487138850560, 5657351404992422784, 3650552739370519680 and 1316268323580640256, the latter studied by [Barber et al. \(2014\)](#) who confirmed the IR excess arises due to the contamination of a background object.

From the final list of 110 selected WD candidates, 77 benefit from IR photometry at both near and mid IR wavelengths and 33 just at mid IR wavelengths. Tables 3-4 list the 77 WD selected candidates with available near and mid IR photometry, 52 of which are new discoveries not yet known to host disks, brown dwarf or low-mass companions. The effective temperatures and radii (derived from the Stefan-Boltzmann equation) associated to the IR contribution's sources are estimated from the composite SED fitting. For this, VOSA uses a range of values around the white dwarf T_{eff} and $\log g$ obtained from the single best fit using the [Koester \(2010\)](#) models together with a blackbody with $T_{\text{eff}} < 5,000$ K. For WDs, the errors in effective temperatures arising from the composite SED fitting are given by the step of the grid of models, which changes with T_{eff} . The step in the grid of blackbody models is set to 25 K.

Table 5 summarizes the information of the 33 targets having only IR photometry at mid IR wavelengths. The SEDs of these IR-excess candidates are poorly populated and hence it is difficult to assess whether or not the detected excesses are real. Another important issue of only having at hand mid IR photometry is that it is hard to assess if the excesses arise from a dust disk or a companion. It is worth noting that for one of them (*Gaia* ID 128198912443928691) the IR excess has been confirmed to arise due to a circumbinary disk ([Farihi et al. 2008b](#)). However, to avoid including a large number of potential false positive detections in our list, these WDs will not be considered further in this work.

More information about the final 77 selected candidates for displaying IR excess with available photometry at both near and mid IR wavelengths, including a visualization of

Table 2. List of 12 binary/multiple co-moving pairs found in this work.

Identifier	Source	Comment
eps Ret	Farihi et al. (2011)	(1)
eps Ret B		
eps Ret b		
PM J04032+2520	Limoges et al. (2015)	(2)
PM J04032+2520E		
2MASS J04031652+2520192		
EGGR 576	Gianninas et al. (2011)	WD+WD
EGGR 577		
LP 402-28	Simbad	WD+WD
LP 402-29		
SDSS J230249.37+243027.9	Simbad	(3)
SDSS J230250.37+243013.3		
L 462-56A	Simbad	WD+WD
L 462-56B		
Gaia 2751252493861856000	El-Badry & Rix (2018)	WD+WD (4)
Gaia 2751252489566343680		
Gaia 3404213863611804672	El-Badry & Rix (2018)	WD+WD (4)
Gaia 3404213863614488192		
Gaia 4209104513139995136	this work	WD+WD (5)
Gaia 4209104577563403136		
Gaia 4659809928696442368	this work	WD+WD (5)
Gaia 4659809928696442496		
Gaia 4964509614631078400	El-Badry & Rix (2018)	WD+WD (5)
Gaia 4964509614631078272		
Gaia 5184384997855024384	this work	WD+WD (5,6)
Gaia 5184385002150373632		

- (1): Binary system formed by a red giant (K2 III) with a confirmed extra-solar planet and a white dwarf (DA3).
 (2) Triple system formed by two white dwarfs and a M-dwarf.
 (3) WD+high proper motion object.
 (4): Both components included in [Jiménez-Esteban et al. \(2018\)](#).
 (5): First component included in [Jiménez-Esteban et al. \(2018\)](#). WD nature of the second component derived from its position in a M_G vs $G-G_{\text{RP}}$ diagram.
 (6): With a $G-G_{\text{RP}} = 0.92$, the second component is one of the coolest WDs in our sample.

their SED fitting, can be found at the SVO archive of WDs with IR excess from *Gaia* DR2⁶.

3 METHODOLOGY ASSESSMENT

The efficiency of our methodology was assessed using the false negative rate, i.e. the fraction of known IR-excess WDs that were not rediscovered in our search. In particular, we compiled a list of 24 WDs at less than 100 pc and with IR excess confirmed by Spitzer. 20 objects (83%) were identified using our methodology and are included in Tables 3-5. The remaining four objects were not identified due to the following two reasons:

(1) Contamination of the WISE photometry due to the presence of a nearby source (WD1929+011 and WD0950-572). It is worth noting that these two objects are not included in the SEIP Spitzer catalogue, otherwise VOSA would have very likely detected the IR excess.

(2) Unreliable WISE photometry in W3 and W4 bands (WD2132+096 and WD2328+107). These targets are not

⁶ <http://svo2.cab.inta-csic.es/vocats/v2/wdw3>

Table 3. List of the 77 WDs found in this work displaying IR excess and with at least three photometric points spread out between near and mid IR wavelengths. 52 are new discovery candidates. Effective temperatures were calculated as described in Sect. 2 while coordinates have been taken from the SVO archive of White Dwarfs from *Gaia*. Surface gravities and masses are obtained as described in Sect. 5. Note the blackbody radii provided for the dusty WDs have no physical meaning. For WDs, the errors in effective temperatures are given by the step of the grid of models, which changes with T_{eff} . The step in the grid of blackbody models is set to 25 K. The second-last column indicates the expected cause of the IR excess (either circumstellar disk or companion; in italics) resulting from the visual SED inspection. The last column indicates the same but based on the IR colours (Fig. 2) and the mass of the WD (in italics; note the classification based on the WD mass is only provided for four low-mass WDs expected to be in close binaries and it is indicated after the IR colour classification following /). Also indicated are the confirmed disks and brown dwarfs by other studies. In these cases the classifications are not given in italics. In bold face we indicate the assumed final classification for each object.

Gaia ID	RA (ICRS)	DEC (ICRS)	Name	T_{eff} (WD)	T_{eff} (bb)	R (bb)	logg (WD)	Mass (WD)	Ref.	Type	Type
DR2	deg	deg		K	K	R_{\odot}	dex	M_{\odot}		SED	other
2416481783371550976	1.8951	-16.0921	EGGR 509	12000±125	2450	0.07	7.84	0.52		<i>comp.</i>	<i>disk</i>
2798132572998105984	1.9484	19.8568		12250±125	2500	0.02	7.75	0.48		comp.	?
367949367212923392	12.3001	38.6918	LAMOST J004912.04+384129.8	9500±125	850	0.23	7.76	0.48		?	
2529337507976700928	12.6909	-3.4487		20000±310	1050	0.10	8.92	1.20		disk	
5026963661794939520	17.1503	-32.6288	HE 0106-3253	15750±125	1900	0.06	7.97	0.60	(Fa10)	<i>disk</i>	disk
2354670057156360576	17.3882	-19.0215		14250±125	550	0.48	7.93	0.57	(De17)	?	
4913589203924379776	18.0888	-56.2411	JL 234	18250±125	950	0.18	7.89	0.56	(Gi12)	<i>disk</i>	disk
2593884960855727872	21.2525	18.1945		8750±125	1700	0.05	8.32	0.79		disk	<i>disk</i>
2588874825669925504	23.8868	14.7649	LSPM J0135+1445	8250±125	2450	0.06	7.50	0.37	(St13)	<i>comp.</i>	BD/comp.
5135466183642594304	26.8412	-21.9477	GD 1400	12000±125	2500	0.06	8.11	0.67	(Fa04)	<i>comp.</i>	BD
291057843317534464(*)	26.9784	23.6617	WD 0145+234	12500±125	-	-	7.99	0.60		disk	<i>disk</i>
95297185335797120	27.2377	19.0405	Wolf 88	13250±125	2200	0.06	8.29	0.78	(Fa09)	<i>disk</i>	disk
4632284754595134080	31.3539	-79.6844		9500±125	800	0.14	8.09	0.65		disk	<i>disk</i>
2489533370280291584	35.8356	-4.9852		10250±125	600	0.45	8.05	0.63		disk	
2489275328645218560	38.5646	-4.1026		13500±125	900	0.16	8.12	0.67		disk	<i>disk</i>
5187830356195791488	45.7209	-1.1429	GD 40	14500±125	950	0.16	8.16	0.70	(Ju07)	<i>disk</i>	disk
139331247344776832	47.0822	36.4914		7500±125	1650	0.01	7.94	0.56		?	
4833891614684676736	52.3630	-47.6435		9750±125	1450	0.06	7.84	0.52		disk	<i>disk</i>
542865797290276352	54.1894	70.7364		10500±125	2800	0.03	7.99	0.60		?	
3251748915515143296	62.7590	-3.9735	GD 56	14500±125	950	0.45	8.00	0.61	(Ju07)	<i>disk</i>	disk
4837423353408638080	63.2121	-45.1696		14000±125	1350	0.08	8.02	0.62		disk	<i>disk</i>
4653404070862114176	64.9077	-73.0623	[DI91] 1592	18250±125	1350	0.02	7.92	0.58	(Ho13)	disk	
271992414775824640	66.0653	52.1696	KPD 0420+5203	15250±125	1100	0.18	8.09	0.67	(Ba16)	<i>disk</i>	disk
152740654933891072	68.4777	28.4579	PM J04339+2827	14000±125	1850	0.02	7.92	0.57	(Xu15)	<i>comp.</i>	BD
203931163247581184	69.6641	41.1585	GD 61	14250±125	1350	0.001	8.08	0.66	(Fa 11)	<i>disk</i>	disk
2986304298645920384	75.3165	-15.1900		11250±125	2350	0.05	7.83	0.51		?	
3415788525598117248	77.5087	23.2613	LAMOST J051002.11+231541.0	17250±125	1200	0.13	8.11	0.68		disk	<i>disk</i>
4799224635833122304	82.7521	-45.9670		10750±125	850	0.13	8.02	0.61		disk	
4795556287084999552	84.4726	-47.9681	EC 05365-4759	18250±125	450	1.40	7.87	0.55	(De16)	<i>disk</i>	disk
3329569015639064192(*)	90.6529	9.07322	LSPM J0602+0904	6000±125	-	-	7.50	0.35		<i>disk</i>	*/ <i>comp.</i>
962995581174346112	90.7863	45.3077		14750±125	1950	0.04	7.95	0.58		disk	<i>disk</i>
3112786176370258688	105.6910	0.0552		11750±125	750	0.14	8.03	0.62		disk	<i>disk</i>
5490140356700680576	108.6243	-55.6572		9000±125	2700	0.07	7.64	0.43		<i>comp.</i>	BD/comp.
872009447786700672(*)	112.5000	27.2781	LSPM J0730+2716W	9250±125	-	-	7.98	0.59		disk	<i>disk</i>
5292685793681027968	113.6708	-60.1979		9250±125	800	0.12	8.24	0.74		disk	<i>disk</i>
1081504483467714176	120.6156	56.5321		10750±125	950	0.16	8.06	0.64		disk	<i>disk</i>
585513959248023936	141.1386	5.3519		6000±125	950	0.09	8.18	0.70		disk	
5662556012001458944	141.2082	-24.38456	0.23	8500±125	700	0.24	7.96	0.57		disk	<i>disk</i>
5740372469987778304	143.4221	-10.0026		8000±125	1450	0.06	8.56	0.95		?	
5459131788043369344	154.3688	-32.6025		8000±125	1300	0.05	7.93	0.56		disk	<i>disk</i>
3888723386196630784	154.5154	15.8660	PG 1015+161	21000±500	1600	0.01	7.98	0.61	(Ju07)	<i>disk</i>	disk
3810933247769901696	169.8012	2.3426	GD 133	12250±125	900	0.17	8.01	0.61	(Ho13)	<i>disk</i>	disk
771517005584473600	171.424	42.3930	GD 308	9500±125	1400	0.06	8.14	0.68	(De11)	disk	<i>disk</i>
3571559292842744960	178.3134	-15.6104	EC 11507-1519	11000±125	750	0.53	7.90	0.55	(Ho13)	<i>disk</i>	disk
3543074313820703488	178.5127	-19.2376		7250±125	750	0.28	7.77	0.48		disk	
3479615106870788864(*)	178.5145	-31.0292		6250±125	-	-	8.17	0.69		disk	<i>disk</i>
4028120776036373760	180.4780	34.0154	SDSS J120154.70+340055.9	6000±125	1300	0.06	8.14	0.67		?	
1692520339315508224	184.2221	74.9237		6500±125	1250	0.05	8.00	0.59		disk	<i>disk</i>
3903151246497510784	190.1509	9.5361		6750±125	750	0.14	8.45	0.87		disk	
3663900436870097664	208.7495	1.1387	SDSS J135459.89+010819.3	11500±125	750	0.20	7.88	0.54		disk	<i>disk</i>
1494157691363079168(*)	217.1406	44.0630		7500±125	-	-	8.36	0.81	(De11)	disk	<i>disk</i>
1488904946359359488	222.5277	40.9264	CBS204	13500±125	800	0.21	7.88	0.54		?	
1183473535423719296	227.4253	14.1892		6250±125	1250	0.04	8.15	0.67		disk	<i>disk</i>
6315417253178248960	229.6198	-11.8109		10250±125	700	0.23	7.86	0.52		disk	

Table 4. List of the 77 WDs found in this work displaying IR excess and with at least three photometric points spread out between near and mid IR wavelengths (cont.).

Gaia ID	RA	DEC	Name	T_{eff}	T_{eff}	R	logg	Mass	Ref.	Type	Type
DR2	(ICRS)	(ICRS)		(WD)	(bb)	(bb)	(WD)	(WD)		SED	other
	deg	deg		K	K	R_{\odot}	dex	M_{\odot}			
1641326979142898048	235.4372	64.8978	V* KX Dra	11000±125	850	0.27	7.90	0.55	(Ki12)	<i>disk</i>	disk
1429618420396285952	243.3191	55.3572	SBSS 1612+554	11250±125	950	0.16	8.06	0.64		<i>disk</i>	<i>disk</i>
4390134326651497728	260.957	4.9799	PM J17238+0458	8500±125	550	0.35	7.94	0.56		<i>disk</i>	<i>disk</i>
1368236912466084352(*)	265.7298	51.6024	SDSS J174255.14+513608.4	8750±125	-	-	7.95	0.57		<i>disk</i>	<i>disk</i>
4583221109793391232(*)	271.6897	27.5299		6500±125	-	-	8.09	0.64		<i>disk</i>	<i>disk</i>
6417955993895552128	273.5734	-73.9174		7750±125	700	0.80	8.06	0.63		<i>disk</i>	?
2155960371551164416	285.8315	60.5980	GD532	10750±125	850	0.23	8.04	0.63		<i>disk</i>	
6429048245152936320	305.0718	-65.4240		6500±125	1900	0.05	8.25	0.74		<i>comp.</i>	?
1837948790953103232	315.1447	21.3826		15250±125	1000	0.44	7.91	0.59		<i>disk</i>	?
6462911897617050240	319.9055	-55.8382	LAWD 84	9500±125	650	0.10	8.02	0.61	(Fa09)	<i>disk</i>	disk
6580498481454705408	320.3473	-42.1484		7500±125	600	0.26	8.32	0.79		<i>disk</i>	
6811977801160882944	328.3816	-26.4821		14750±125	700	0.23	9.09	1.31		<i>disk</i>	
2677851743291189888	335.1279	-0.6854	PHL 5038	7500±125	1050	0.12	7.87	0.53	(De11)	<i>disk</i>	<i>disk</i>
2595728287804350720	336.0726	-16.2631	PHL 5103	10000±125	1450	0.04	8.12	0.67	(Ro15)	<i>disk</i>	disk
1900545847646195840	337.4920	30.4028	PM J22299+3024	10500±125	2550	0.08	7.41	0.35		<i>comp.</i>	<i>disk/comp.</i>
2622979271185741312	338.3480	-6.0278		8250±125	850	0.31	8.07	0.63		<i>disk</i>	
6594180460552162944	338.477	-38.5436	LP 1033-28	8500±125	1000	0.07	8.05	0.62		<i>disk</i>	<i>disk</i>
2712240064671438720	344.3588	7.9285	G28-27	13750±125	950	0.07	9.36	1.44	(De11)	<i>disk</i>	
1995097319287822080	346.3820	51.4227		12750±125	1800	0.04	7.93	0.57		<i>disk</i>	<i>disk</i>
6499095244738784128	349.0564	-55.4912		10250±125	950	0.10	8.35	0.81		<i>disk</i>	<i>disk</i>
2660358032257156736	352.1975	5.2478	V* ZZ Psc	10750±125	950	0.19	7.90	0.55	(Re05)	<i>disk</i>	disk
1923682286712356992	352.9001	41.0248	EGGR 160	14500±125	700	0.36	7.94	0.58	(Ho13)	<i>disk</i>	disk
6538863343364422528	355.1527	-37.1458	EC 23379-3725	12250±125	700	0.41	7.74	0.48		<i>disk</i>	<i>disk</i>

Comments: (*) Marginal IR excess. No reliable values of blackbody effective temperature and radius.

References: (Fa10): Farihi et al. (2010), (Gi12): Girven et al. (2012), (St13): Steele et al. (2013) (Fa04): Farihi & Christopher (2004) (Fa09): Farihi et al. (2009), (Ju07): Jura et al. (2007), (Ho13): Hoard et al. (2013), (Ba16): Barber et al. (2016), (Xu15): Xu et al. (2015) (Fa11): Farihi et al. (2011), (De16): Dennihy et al. (2016), (Fa08): Farihi et al. (2008a), (Ki12) Kilic et al. (2012), (De11): Debes et al. (2011), (De17): Dennihy et al. (2017) (Re05): Reach et al. (2005). (Ro15): Rocchetto et al. (2015).

included in the SEIP Spitzer catalogue neither, hence VOSA could not detect the IR excess.

These results confirm the robustness of our methodology (a success rate of 83%) to identify WDs with IR excess. We therefore assume our IR-excess sample to be 83% complete. It is also important to note that if we take into account that the four objects that we could not recover were identified from publicly unavailable Spitzer data (i.e. data not included in the SEIP catalogue), then the success rate of our method would increase to 100%.

Assuming an IR-excess completeness of 83% for our sample does not imply that we have discovered 83% of all WDs displaying IR excess within 100 pc from the Sun. First, we are basing our methodology assessment on *confirmed* WDs with IR excess by Spitzer, therefore there may exist WDs without Spitzer data and displaying IR excess that we are not taking into account and that are consequently missed by this and all previous studies. Second, and more important, we are only considering 3,733 objects with reliable IR photometry and with $G_{\text{BP}} - G_{\text{RP}}$ colours below 0.8 mag within our Gaia 100 pc sample.

4 CHARACTERIZATION OF THE SAMPLE

It is widely accepted that there are three main possibilities to explain the IR excess detections in WDs such as those listed in Tables 3-4: the presence of a brown dwarf companion, the presence of low-mass stellar companion and the existence

of a circumstellar dust disk. To discern the origin of the IR excess we follow two different approaches, namely the use of a colour-colour diagram and the visual inspection of the SEDs. The classification of IR-excess origin based on these two methods are provided in the last and second-last columns of Tables 3-4, respectively.

We use the colour-colour diagram proposed by Barber et al. (2014). Fig.2 compares the IR colours of the 54 WDs with excess included in Tables 3-4 and with good 2MASS (Qflg \neq U in the J and H bands) and WISE (ccf=0 and qph=A/B in the W2 band) photometry to those of M, L, T dwarf stars and brown dwarfs. 15 objects (pink bullets in Figure 2) have been classified as dusty WDs in the literature, while for one object (green bullet) the IR excess has been ascribed to the presence of a BD companion. 31 objects (black bullets) are located well apart from the stellar/brown dwarf loci, and we hence classify them as dusty WDs based on their IR colours. Two objects (yellow bullets) lie either near the brown dwarf locus or near a confirmed WD+BD binary as we thus classify them as WD+BD candidates. For one of these objects (Gaia ID: 152740654933891072) the morphology flag of the UKIDSS catalogue indicates the possibility that this source was extended at more than one bandpass, which is an additional evidence supporting the hypothesis that the IR excess is due to nearby brown dwarf. The remaining five (black triangles) lie in colour regions expected for T brown dwarfs where also confirmed dusty WDs are located, therefore it becomes difficult to assess the origin of the IR excess in these objects. We explored their quality

Table 5. List of 33 IR-excess WD candidates with available photometry at only mid IR wavelengths.

Gaia ID	RA	DEC	Name
DR2	(ICRS)	(ICRS)	
	deg	deg	
2741440172922171008	4.2305	5.0786	SDSS J001655.37+050442.1
2858896086675180928	7.2235	30.0918	
2344098385998773120	11.3746	-25.0516	
377520826387065856	13.0183	45.0927	
306805388153226368	16.7916	27.1691	
306350606950880128	16.8592	25.3099	
2790417540424293120	16.9558	21.1294	SDSS J010749.34+210745.2
5161531373793965440	49.6922	-13.0005	
568168544844912128	57.0280	80.8102	
4887631143142117632	57.4624	-30.5289	
498487545190443136	89.8444	72.9873	
992771180686912000	98.8498	52.2593	
921804126089222784	122.9556	42.2025	KUV 08084+4221
1118374024628715264	129.4702	69.2181	
1051954485699665280 ¹	152.5329	61.9211	
738060065046666240	163.0523	33.3884	
789712823515276416	169.3462	48.8665	
3705386281897262848	193.0632	4.1786	HS 1249+0426
3938156295111047680	196.4251	18.0179	V* GP Com
1281989124439286912 ²	224.5277	29.6223	EGGR 298
1157317008497672320	227.7374	6.4638	SDSS J151056.99+062749.7
1219699145026398848	237.2293	24.8536	SDSS J154855.04+245112.9
1316607896578157824 ³	240.4179	27.5969	LSPM J1601+2735
1199686173677816576 ¹	242.1648	17.3935	
1428562506980546688	244.1432	54.1698	
4555079659441944960	262.1905	20.8949	
6845706900891884928	303.9679	-28.5888	
6886271973655421824	312.8046	-15.3495	
6809396800693752576	314.4396	-20.0568	
6884996230921934976	316.6775	-14.7588	
2284456545980836736	319.6924	76.9831	
1946495125767488896	326.3801	32.8618	
2199338643594260352	329.6359	58.0752	Lan 432

References: (2): [Farihi et al. \(2008a\)](#), (1): [Debes et al. \(2011\)](#), (3): [Dennihy et al. \(2017\)](#)

flags associated to the *Gaia* astrometry. Following the latest recommendations published by the *Gaia* ESA team in the *Known issues with the Gaia DR2 data* web page⁷, we defined sources with good astrometry as those having the re-normalised unit weight error (RUWE) < 1.4. Sources having a higher value of RUWE may have a worse astrometric solution due to different effects, one of those being the presence of a close companion. However, we got a value of RUWE < 1.4 for the five objects, which prevented us from discriminating between a disk or brown dwarf/low-mass star origin of their IR excesses.

In order to further explore the origin of the IR excesses we visually inspected the SEDs of the 77 candidates. Eight of them benefit only from J 2MASS and WISE photometry, hence we do not have enough information at hand to reach a conclusion. In these cases we flag the origin of the excess as unknown (? in the second last column of Tables 3-4). For eight additional objects the IR excesses arise at the J and/or H bands, which supports the idea of these WDs being in binary systems with either low-mass stars or brown dwarf com-

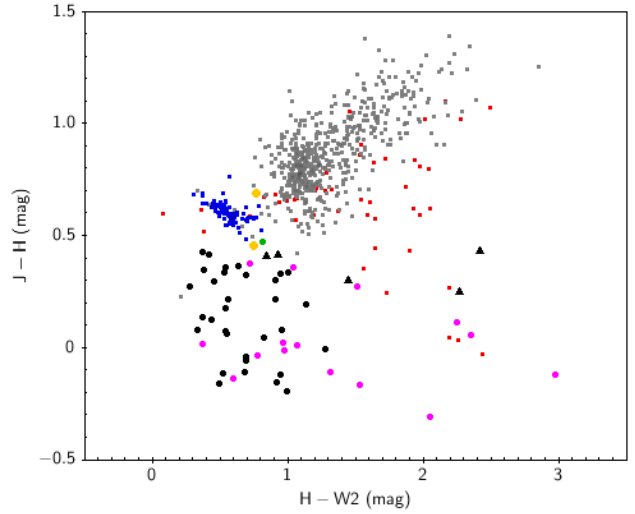


Figure 2. *J-H* vs *H-W2* colour-colour diagram showing the loci of stars and brown dwarfs of M (blue squares), L (grey squares) and T (red squares) spectral types. M dwarfs have been taken from [Reiners et al. \(2018\)](#) while L,T objects are from [Smart et al. \(2017\)](#). Bullets represent the 54 WDs with IR excess listed in Tables 3-4 with good 2MASS and WISE photometry. Pink bullets (15) represent objects classified as confirmed dusty WDs in the last column of Tables 3-4, while green bullets (1) are objects classified as confirmed WD+BD systems in the same column. Black (31) and yellow (2) bullets are objects classified as dusty WDs or WD+BD systems, respectively according to their position in the diagram. Black triangles (5) represent objects for which the origin of the IR excess is uncertain.

panions. Two objects (*Gaia* IDs 2588874825669925504 and 5135466183642594304) are in fact confirmed, and one more (152740654933891072) is a candidate to harbour a brown dwarf based on its IR colours (Fig. 2). These objects are flagged to harbour companions in the second-last column of Tables 3-4 and we include the brown dwarf classification of the three discussed targets in the last column of the same tables. The SEDs of 61 WDs display IR excess at K-band or longer wavelengths, characteristic features of circumstellar disk candidates. These objects are hence flagged as such in the second-last column of Tables 3-4.

5 DISCUSSION

We have identified 77 IR-excess WD candidates within the 100 pc *Gaia* WD catalogue, 52 of which have not been published before (see Tables 3-4). The WD effective temperatures are derived fitting the photometric SED of each WD using VOSA (Section 2), which together with the bolometric luminosities (also provided by VOSA by making use of the *Gaia* parallaxes) yield the radii of the WDs from the Stefan-Boltzmann equation. The WD masses are estimated interpolating the radii and effective temperatures obtained in this way in the WD cooling tracks for hydrogen-rich, DA, atmospheres of [Renedo et al. \(2010\)](#), following our procedure described in [Jiménez-Esteban et al. \(2018\)](#). Given that *Gaia* DR2 does not provide stellar spectra, the reliability of the determined masses relies on the assumption that all our WDs are DAs. As we showed

⁷ <https://www.cosmos.esa.int/web/gaia/dr2-known-issues>

in Jiménez-Esteban et al. (2018), the contribution of DB (helium-rich) WDs to the sample of WDs with determined stellar parameters should be no higher than $\approx 6\%$. The average uncertainties that are introduced when assuming DA models when deriving the effective temperatures and masses of DB WDs are 1700 ± 1680 K and $0.08 \pm 0.06 M_{\odot}$, respectively, where the errors are the standard deviations. These values are obtained comparing the stellar parameters calculated by Jiménez-Esteban et al. (2018) for 152 common SDSS DB WDs in the spectroscopic catalogue of Koester & Kepler (2015) with relative error below 10% in effective temperature and surface gravity errors below 0.05 dex.

Four WDs have determined masses under $0.45 M_{\odot}$, which indicates these objects are likely members of close binaries with sub-stellar or low-mass companions (from which the IR excess likely arises) that formed through common envelope evolution. Another possibility is that these are non-DA WDs, in which case the masses cannot be considered as reliable. The four potentially low-mass WDs have the following *Gaia* IDs: 2588874825669925504 (LSPM J0135+1445), 3329569015639064192 (LSPM J0602+0904), 5490140356700680576, 1900545847646195840 (PM J22299+3024). LSPM J0135+1445 is a confirmed WD+BD binary (Steele et al. 2013). 3329569015639064192 is classified as a disk candidate based on its SED, which supports the idea of this WD being of a non-DA spectral class. 5490140356700680576 is classified as a companion and brown dwarf by its SED and IR colours, respectively, which strongly indicates this WD is indeed part of a close binary. Finally, the SED and IR colours of 1900545847646195840 indicate a companion and disk origin, respectively, and therefore more information is required (e.g. IR spectroscopy) to confirm this WD is in a close binary system.

The effective temperature and mass distributions for the 60 WDs in which the IR excess is confirmed/expected to arise from the presence of a circumstellar dust disk (indicated in bold face in the last two columns of Tables 3–4) are illustrated in Fig. 3. Inspection of the Figure reveals the effective temperatures are concentrated between 6,000–20,000 K, with a peak at $\approx 9,000$ K. No WDs are found below 6,000 K due to the $G_{BP} - G_{RP} < 0.8$ mag cut we imposed in Section 2. The drop of IR-excess WD candidates above $\approx 20,000$ K is in line with previous studies (e.g. Bergfors et al. 2014; Barber et al. 2014, 2016). The physical mechanism causing this could be that the accretion of the material onto the WD is supplied by a pure gas disc, which results from the sublimation of optically thin dust due to the high effective temperatures (Bonsor et al. 2017). A drop in the fraction of IR-excess WDs below $\approx 8,000$ – $10,000$ K is also reported in previous works (e.g. Bergfors et al. 2014), a result that favours a positive correlation between the WD effective temperature and the detection of IR-excess. In the top-left panel of Fig. 3 one can clearly see the same tendency, i.e. the fraction of cool ($\lesssim 8,000$ – $10,000$ K) WDs displaying IR excess decreases. However, since the *Gaia* 100pc WD sample is volume-limited and hence dominated by WDs cooler than 10,000 K (Jiménez-Esteban et al. 2018), the peak of the effective temperature distribution occurs at $\approx 9,000$ K rather than at higher temperatures (see the top-right panel of Figure 3).

The mass distribution of the WD candidates for displaying IR excess due to a circumstellar dust disk is clearly

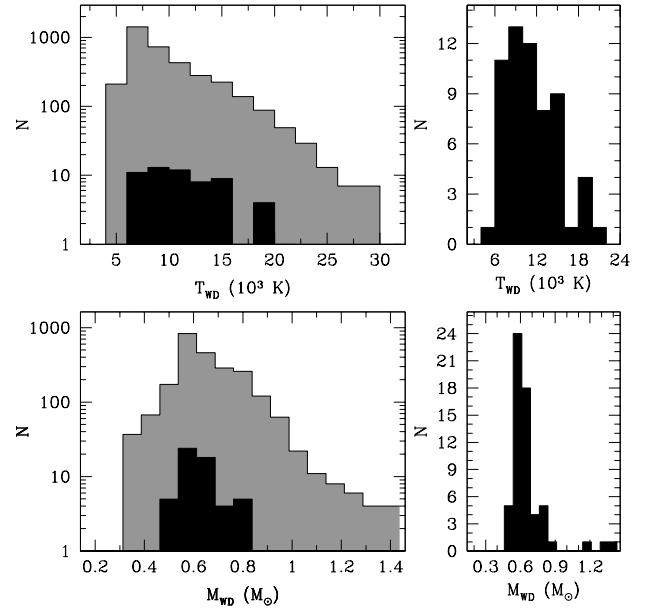


Figure 3. Left panels: WD effective temperature and mass distributions in logarithmic scale. In gray we show the entire 100 pc sample of *Gaia* WDs with reliable IR photometry, in black those WD candidates to show IR excess due to a circumstellar disk (Tables 3–4). Right panels: the parameter distributions in linear scale of the WD candidates to show IR excess due to the presence of a circumstellar disk. The WD masses above $1 M_{\odot}$ should be taken with caution, especially for those objects displaying IR excess, since these are possibly non-DA WDs.

dominated by $\approx 0.6 M_{\odot}$ objects. Indeed, $\approx 50\%$ of the objects have masses between 0.55 and $0.65 M_{\odot}$. It is worth mentioning that three WDs have masses above $1 M_{\odot}$, one of them near the Chandrasekhar mass limit. The masses of these WDs should be taken with caution since there exists the possibility these are non-DAs. WDs more massive than $> 0.8 M_{\odot}$ are not generally found to display IR excess (Mullally et al. 2007; Barber et al. 2016). This is also observed in our mass distribution, where only $\approx 5\%$ of the objects are located in the 0.8 – 1.0 mass range.

Based on the 60 confirmed/expected dusty WDs in Tables 3–4, we calculate a fraction of IR-excess WDs due to the existence of a circumstellar dust disk of $1.6 \pm 0.2\%$ ⁸. As we have already mentioned, the detection of IR-excess seems to be positively correlated with the WD effective temperature. Thus, if we exclude all WDs with effective temperatures below 8,000 K from our sample, the fraction of IR-excess WDs increases to $2.3 \pm 0.3\%$, as expected. For completeness, we provide the fractions at different effective temperature bins in Table 6, where one can see the values gradually decrease as soon as we move towards cooler effective temperatures. The fractions we derived are in excellent agreement with the 1–5% measured percentages by other studies (Debes et al. 2011; Barber et al. 2016; Bonsor et al. 2017; Wilson et al. 2019). It has to be emphasised however that these values should be considered as lower limits, since many WDs in

⁸ The error is calculated as $\sqrt{\frac{frac \times (1 - frac)}{N_{tot}}}$, where N_{tot} is the total number of WDs and $frac$ is the IR-excess fraction of WDs.

Table 6. The fraction of IR-excess WDs due to the existence of a circumstellar dust disk for different effective temperature bins.

T_{eff} range (K)	fraction (%)	error (%)
6,000-8,000	0.8	0.2
8,000-10,000	1.8	0.5
10,000-12,000	2.8	0.8
12,000-14,000	2.9	1.0
14,000-16,000	4.0	1.3
16,000-18,000	0.7	0.7
18,000-20,000	4.5	2.2
20,000-22,000	2.0	2.0

our sample with reliable IR photometry have no counterparts at near IR wavelengths (we remind the reader that all our candidates have reliable IR photometry at both near and mid IR wavelengths). Of the 3,733 WDs in our analysed sample, 2802 have near and mid IR counterparts. This implies a revised overall WD IR-excess fraction of $2.1 \pm 0.3\%$. Moreover, if we take into account that we assumed our IR-excess sample to be 83% complete (Section 3), this implies a completeness-corrected fraction of $2.6 \pm 0.3\%$.

Our sample of 77 IR-excess WD candidates contains two confirmed WD+BD binaries (LSPM J0135+1445 and GD 1400) and two more that are also likely to harbour brown dwarf companions: PM J04339+2827 (Gaia ID=54901403567006805) and 549014035670068057 (yellow dots in Fig. 2). We thus derive a fraction of IR-excess WDs due to brown dwarf companions of $0.10 \pm 0.05\%$. If we assume that the IR excess of all WDs expected to harbour companions in Tables 3-4 is due to a brown dwarf rather than due to a low-mass star, the percentage increases to $0.20 \pm 0.05\%$, or $0.23 \pm 0.05\%$ if we take into account the incompleteness of our sample. Our results are in agreement with the expected value of $<0.5\%$ claimed by Farihi et al. (2005).

Finally, it is worth mentioning that all IR-excess WD candidates found in this study are classified to be members of the Galactic thin disk, according to the Random Forest identification algorithm we presented in Torres et al. (2019). The proportion of WDs within the *Gaia* 100 pc sample belonging to the thin/thick disk within the colour limits considered ($G_{\text{BP}} - G_{\text{RP}} < 0.8$ mag) is expected to be 96.5:3.5 (Torres et al. 2019), which translates into an expected number of ≈ 74 thin disk and ≈ 3 thick disk IR-excess WDs among our 77 identified objects. Thus, the expected number of thick disk WDs is at odds with the observed value. Given that thick disk WDs are generally old (≥ 9 Gyr), and taking into account that the fraction of IR-excess WDs drops for cooler (hence generally older) objects, the discrepancy between the expected and the observed number of thin/thick disk IR-excess WDs seems to be naturally explained.

6 CONCLUSIONS

We have analysed the SEDs of 3,733 WDs within 100pc from the *Gaia* volume-limited sample of Jiménez-Esteban et al. (2018) with reliable IR photometry and with $G_{\text{BP}} - G_{\text{RP}}$ colours below 0.8 mag with the aim of detecting IR excess candidates. The search has resulted in 77 identifications, 52 of which are new. 33 additional WDs have been also identified as potential IR-excess candidates. However, the fact that no near IR photometry is available in these cases makes

the reliability of the detections less certain. We have provided the largest volume-limited sample of IR excess WD candidates to date, which represents a fraction of $2.6 \pm 0.3\%$ of the sample analysed in this work. Having this large number of WD candidates for harbouring a circumstellar disk at hand opens up the possibility to considerably increase our understanding of the properties of extreme planetary systems. A similar exercise to the one performed in this work but for the entire *Gaia* sample of WDs is encouraging. Even though the *Gaia* WD catalogue including WDs at all distances is magnitude- rather than volume-limited, such an analysis would result in the identification of many additional WDs displaying IR-excess, important for future follow-up studies.

ACKNOWLEDGEMENTS

This work has made use of data from the European Space Agency (ESA) mission *Gaia* (<https://www.cosmos.esa.int/gaia>), processed by the *Gaia* Data Processing and Analysis Consortium (DPAC, <https://www.cosmos.esa.int/web/gaia/dpac/consortium>). Funding for the DPAC has been provided by national institutions, in particular the institutions participating in the *Gaia* Multilateral Agreement. This publication makes use of VOSA, developed under the Spanish Virtual Observatory project supported from the Spanish MINECO through grant AyA2017-84089. This research has made use of the SIMBAD database, operated at CDS, Strasbourg, France. We acknowledge use of the ADS bibliographic services. This research has made use of "Aladin sky atlas" developed at CDS, Strasbourg Observatory, France. This research has made use of Topcat (Taylor 2005). ARM acknowledges support from the MINECO under the Ramón y Cajal programme (RYC-2016-20254). ARM and ST acknowledge support from the AYA2017-86274-P grant and the AGAUR grant SGR-661/2017. F.J.E. acknowledges financial support from the Spacetec-CM project (S2013/ICE-2822), and from ASTERICS project (ID:653477, H2020-EU.1.4.1.1. - Developing new world-class research infrastructures). We thank the anonymous referee for her/his suggestions and comments.

APPENDIX A: ONLINE CATALOGUE SERVICE

In order to help the astronomical community on using the catalogue of WDs with infrared excess identified in this work, we have developed an archive system that can be accessed from a webpage⁹ or through a Virtual Observatory ConeSearch¹⁰.

The archive system implements a very simple search interface that permits queries by coordinates and range of effective temperatures, surface gravities and masses. The user can also select the maximum number of sources to return (with values from 10 to unlimited).

The result of the query is a HTML table with all the

⁹ <http://svo2.cab.inta-csic.es/vocats/v2/wdw3>

¹⁰ e.g. <http://svo2.cab.inta-csic.es/vocats/v2/wdw3/cs.php?RA=1.895&DEC=16.092&SR=0.1&VERB=2>

sources found in the archive fulfilling the search criteria. The result can also be downloaded as a VOTable or a CSV file. Detailed information on the output fields can be obtained placing the mouse over the question mark (“?”) located close to the name of the column. The archive also implements the SAMP¹¹ (Simple Application Messaging) Virtual Observatory protocol. SAMP allows Virtual Observatory applications to communicate with each other in a seamless and transparent manner for the user. This way, the results of a query can be easily transferred to other VO applications, such as, for instance, Topcat.

REFERENCES

- Alam S., et al., 2015, *ApJS*, **219**, 12
- Allard F., Homeier D., Freytag B., 2012, *Philosophical Transactions of the Royal Society of London Series A*, **370**, 2765
- Althaus L. G., Córscico A. H., Isern J., García-Berro E., 2010, *A&ARv*, **18**, 471
- Badenes C., van Kerkwijk M. H., Kilic M., Bickerton S. J., Mazeh T., Mullally F., Tal-Or L., Thompson S. E., 2013, *MNRAS*, **429**, 3596
- Barber S. D., Patterson A. J., Kilic M., Leggett S. K., Dufour P., Bloom J. S., Starr D. L., 2012, *ApJ*, **760**, 26
- Barber S. D., Kilic M., Brown W. R., Gianninas A., 2014, *ApJ*, **786**, 77
- Barber S. D., Belardi C., Kilic M., Gianninas A., 2016, *MNRAS*, **459**, 1415
- Bayo A., Rodrigo C., Barrado y Navascués D., Solano E., Gutiérrez R., Morales-Calderón M., Allard F., 2008, *A&A*, **492**, 277
- Bergeron P., et al., 2011, *ApJ*, **737**, 28
- Bergfors C., Farihi J., Dufour P., Rocchetto M., 2014, *MNRAS*, **444**, 2147
- Bianchi L., GALEX Team 2000, *Mem. Soc. Astron. Italiana*, **71**, 1123
- Bonnarel F., et al., 2000, *A&AS*, **143**, 33
- Bonsor A., Mustill A. J., Wyatt M. C., 2011, *MNRAS*, **414**, 930
- Bonsor A., Farihi J., Wyatt M. C., van Lieshout R., 2017, *MNRAS*, **468**, 154
- Burleigh M. R., Clarke F. J., Hodgkin S. T., 2002, *MNRAS*, **331**, L41
- Castanheira B. G., Kepler S. O., 2008, *MNRAS*, **385**, 430
- Chambers K. C., et al., 2016, preprint, ([arXiv:1612.05560](https://arxiv.org/abs/1612.05560))
- Cross N. J. G., et al., 2012, *A&A*, **548**, A119
- Dark Energy Survey Collaboration et al., 2016, *MNRAS*, **460**, 1270
- Debes J. H., Sigurdsson S., 2002, *ApJ*, **572**, 556
- Debes J. H., Hoard D. W., Wachter S., Leisawitz D. T., Cohen M., 2011, *ApJS*, **197**, 38
- Debes J. H., Walsh K. J., Stark C., 2012, *ApJ*, **747**, 148
- Dennihy E., Debes J. H., Dunlap B. H., Dufour P., Teske J. K., Clemens J. C., 2016, *ApJ*, **831**, 31
- Dennihy E., Clemens J. C., Debes J. H., Dunlap B. H., Kilkenny D., O’Brien P. C., Fuchs J. T., 2017, *ApJ*, **849**, 77
- Dennihy E., Clemens J. C., Dunlap B. H., Fanale S. M., Fuchs J. T., Hermes J. J., 2018, *ApJ*, **854**, 40
- El-Badry K., Rix H.-W., 2018, *MNRAS*, **480**, 4884
- Farihi J., 2016, *New Astron. Rev.*, **71**, 9
- Farihi J., Christopher M., 2004, *AJ*, **128**, 1868
- Farihi J., Becklin E. E., Zuckerman B., 2005, *ApJS*, **161**, 394
- Farihi J., Zuckerman B., Becklin E. E., 2008a, *ApJ*, **674**, 431
- Farihi J., Becklin E. E., Zuckerman B., 2008b, *ApJ*, **681**, 1470
- Farihi J., Jura M., Zuckerman B., 2009, *ApJ*, **694**, 805
- Farihi J., Jura M., Lee J. E., Zuckerman B., 2010, *ApJ*, **714**, 1386
- Farihi J., Burleigh M. R., Holberg J. B., Casewell S. L., Barstow M. A., 2011, *MNRAS*, **417**, 1735
- Farihi J., Gänsicke B. T., Koester D., 2013, *Science*, **342**, 218
- Gaia Collaboration Brown A. G. A., Vallenari A., Prusti T., de Bruijne J. H. J., Babusiaux C., Bailer-Jones C. A. L., 2018, preprint, ([arXiv:1804.09365](https://arxiv.org/abs/1804.09365))
- Gänsicke B. T., Marsh T. R., Southworth J., Rebassa-Mansergas A., 2006, *Science*, **314**, 1908
- Gänsicke B. T., Koester D., Farihi J., Girven J., Parsons S. G., Breedt E., 2012, *MNRAS*, **424**, 333
- Gentile Fusillo N. P., et al., 2019, *MNRAS*, **482**, 4570
- Gianninas A., Bergeron P., Ruiz M. T., 2011, *ApJ*, **743**, 138
- Girven J., Brinkworth C. S., Farihi J., Gänsicke B. T., Hoard D. W., Marsh T. R., Koester D., 2012, *ApJ*, **749**, 154
- Hewett P. C., Warren S. J., Leggett S. K., Hodgkin S. T., 2006, *MNRAS*, **367**, 454
- Hoard D. W., Debes J. H., Wachter S., Leisawitz D. T., Cohen M., 2013, *ApJ*, **770**, 21
- Hollands M. A., Gänsicke B. T., Koester D., 2018a, *MNRAS*, **477**, 93
- Hollands M. A., Tremblay P.-E., Gänsicke B. T., Gentile-Fusillo N. P., Toonen S., 2018b, *MNRAS*, **480**, 3942
- Jiménez-Esteban F. M., Torres S., Rebassa-Mansergas A., Skorobogatov G., Solano E., Cantero C., Rodrigo C., 2018, *MNRAS*, **480**, 4505
- Jura M., 2008, *AJ*, **135**, 1785
- Jura M., Farihi J., Zuckerman B., 2007, *ApJ*, **663**, 1285
- Kilic M., Patterson A. J., Barber S., Leggett S. K., Dufour P., 2012, *MNRAS*, **419**, L59
- Klein B., Jura M., Koester D., Zuckerman B., Melis C., 2010, *ApJ*, **709**, 950
- Koester D., 2010, *Mem. Soc. Astron. Italiana*, **81**, 921
- Koester D., Kepler S. O., 2015, *A&A*, **583**, A86
- Koester D., Gänsicke B. T., Farihi J., 2014, *A&A*, **566**, A34
- Lada C. J., et al., 2006, *AJ*, **131**, 1574
- Limoges M.-M., Bergeron P., Lépine S., 2015, *ApJS*, **219**, 19
- Mullally F., Kilic M., Reach W. T., Kuchner M. J., von Hippel T., Burrows A., Winget D. E., 2007, *ApJS*, **171**, 206
- Pecauc M. J., Mamajek E. E., 2013, *ApJS*, **208**, 9
- Raddi R., Gänsicke B. T., Koester D., Farihi J., Hermes J. J., Scaringi S., Breedt E., Girven J., 2015, *MNRAS*, **450**, 2083
- Reach W. T., Kuchner M. J., von Hippel T., Burrows A., Mullally F., Kilic M., Winget D. E., 2005, *ApJ*, **635**, L161
- Rebassa-Mansergas A., Gänsicke B. T., Schreiber M. R., Koester D., Rodríguez-Gil P., 2010, *MNRAS*, **402**, 620
- Rebassa-Mansergas A., Ren J. J., Parsons S. G., Gänsicke B. T., Schreiber M. R., García-Berro E., Liu X.-W., Koester D., 2016, *MNRAS*, **458**, 3808
- Reiners A., et al., 2018, *A&A*, **612**, A49
- Ren J. J., et al., 2014, *A&A*, **570**, A107
- Renedo I., Althaus L. G., Miller Bertolami M. M., Romero A. D., Córscico A. H., Rohrmann R. D., García-Berro E., 2010, *ApJ*, **717**, 183
- Rocchetto M., Farihi J., Gänsicke B. T., Bergfors C., 2015, *MNRAS*, **449**, 574
- Siess L., 2007, *A&A*, **476**, 893
- Skrutskie M. F., et al., 2006, *AJ*, **131**, 1163
- Smart R. L., Marocco F., Caballero J. A., Jones H. R. A., Barrado D., Beamín J. C., Pinfeld D. J., Sarro L. M., 2017, *MNRAS*, **469**, 401
- Steele P. R., et al., 2013, *MNRAS*, **429**, 3492
- Taylor M. B., 2005, in Shopbell P., Britton M., Ebert R., eds, *Astronomical Society of the Pacific Conference Series Vol. 347, Astronomical Data Analysis Software and Systems XIV*. p. 29
- Torres S., Cantero C., Rebassa-Mansergas A., Skorobogatov G., Jiménez-Esteban F. M., Solano E., 2019, arXiv e-prints,

¹¹ <http://www.ivoa.net/documents/SAMP/>

- Tremblay P.-E., Bergeron P., 2008, [ApJ](#), **672**, 1144
- Vanderburg A., et al., 2015, [Nature](#), **526**, 546
- Veras D., Mustill A. J., Bonsor A., Wyatt M. C., 2013, [MNRAS](#), **431**, 1686
- Wilson D. J., Gänsicke B. T., Farihi J., Koester D., 2016, [MNRAS](#), **459**, 3282
- Wilson T. G., Farihi J., Gänsicke B. T., Swan A., 2019, [MNRAS](#),
- Wright E. L., et al., 2010, [AJ](#), **140**, 1868
- Wu X., Roby T., Ly L., 2010, in Mizumoto Y., Morita K. I., Ohishi M., eds, *Astronomical Society of the Pacific Conference Series Vol. 434, Astronomical Data Analysis Software and Systems XIX*. p. 14
- Xu S., Jura M., 2012, [ApJ](#), **745**, 88
- Xu S., Jura M., 2014, [ApJ](#), **792**, L39
- Xu S., Jura M., Koester D., Klein B., Zuckerman B., 2014, [ApJ](#), **783**, 79
- Xu S., Jura M., Pantoja B., Klein B., Zuckerman B., Su K. Y. L., Meng H. Y. A., 2015, [ApJ](#), **806**, L5
- Xu S., Zuckerman B., Dufour P., Young E. D., Klein B., Jura M., 2017, [ApJ](#), **836**, L7
- Zuckerman B., Becklin E. E., 1987, [ApJ](#), **319**, L99
- Zuckerman B., Koester D., Reid I. N., Hünsch M., 2003, [ApJ](#), **596**, 477

This paper has been typeset from a $\text{\TeX}/\text{\LaTeX}$ file prepared by the author.